



Fringe instability in constrained soft elastic layers†

Cite this: DOI: 10.1039/c6sm01672c

Shaoting Lin,‡^a Tal Cohen,‡^{bc} Teng Zhang,‡^{ad} Hyunwoo Yuk,^a Rohan Abeyaratne^a and Xuanhe Zhao*^{ac}

Soft elastic layers with top and bottom surfaces adhered to rigid bodies are abundant in biological organisms and engineering applications. As the rigid bodies are pulled apart, the stressed layer can exhibit various modes of mechanical instabilities. In cases where the layer's thickness is much smaller than its length and width, the dominant modes that have been studied are the cavitation, interfacial and fingering instabilities. Here we report a new mode of instability which emerges if the thickness of the constrained elastic layer is comparable to or smaller than its width. In this case, the middle portion along the layer's thickness elongates nearly uniformly while the constrained fringe portions of the layer deform nonuniformly. When the applied stretch reaches a critical value, the exposed free surfaces of the fringe portions begin to undulate periodically without debonding from the rigid bodies, giving the fringe instability. We use experiments, theory and numerical simulations to quantitatively explain the fringe instability and derive scaling laws for its critical stress, critical strain and wavelength. We show that in a force controlled setting the elastic fingering instability is associated with a snap-through buckling that does not exist for the fringe instability. The discovery of the fringe instability will not only advance the understanding of mechanical instabilities in soft materials but also have implications for biological and engineered adhesives and joints.

Received 21st July 2016,
Accepted 4th October 2016

DOI: 10.1039/c6sm01672c

www.rsc.org/softmatter

1. Introduction

Soft elastic layers constrained between relatively rigid bodies appear in biological glues,^{1–4} joints⁵ and engineering applications including sealants, insulators, bearings, and adhesives.^{6,7} When the rigid bodies are pulled apart, the stressed layer can undergo various modes of mechanical instabilities due to a combination of the elastic layer's incompressibility, the mechanical constraints and the applied loads. For example, if the hydrostatic tensile stress in any region of the elastic layer reaches a critical value, a cavity can nucleate and grow in that region, leading to the cavitation instability.^{7–11} If the elastic layer partially debonds from the rigid body, the delaminated interface can undulate periodically to give the interfacial instability.^{12–16} Even if perfect bonding between the elastic layer and the rigid bodies is maintained, the exposed

meniscus can become unstable, forming spatially periodic fingers of air that invade the elastic layer (Fig. 1a).^{17–19} Morphologically the elastic fingering instability resembles the viscous fingering instability in thin fluid layers;^{20–23} however, the elastic and viscous fingering follows different governing laws. Whereas the abovementioned instabilities have been intensively studied in cases where the layer's thickness is much smaller than its lateral dimensions (*i.e.*, length and width), will any mechanical instability occur if the constrained layer's thickness is comparable to or larger than one lateral dimension (*e.g.*, width)?

Here we show that a constrained soft elastic layer with a comparable thickness and width can indeed undergo mechanical instability, which forms on its exposed surfaces but is localized at the constrained fringes of the layer (Fig. 1b). When subjected to tension, the middle portion of the layer elongates nearly uniformly but the constrained fringe portions of the layer deform nonuniformly. As the applied stretch reaches a critical value, the exposed surfaces of the fringe portions begin to undulate periodically without debonding from the rigid bodies, giving the fringe instability (Fig. 1b).

While both the fingering^{17,18} and fringe instabilities occur on the elastic layers' exposed surfaces, the two modes of instabilities are dramatically different. To quantitatively understand the fringe instability and its differences from fingering instability, we combine experiments, theory and numerical simulations to show that: (i) the deformed layer's meniscus, prior to fringe

^a Department of Mechanical Engineering, Massachusetts Institute of Technology, Cambridge, MA 02139, USA. E-mail: zhaohx@mit.edu

^b School of Engineering and Applied Science, Harvard University, Cambridge, MA 02138, USA

^c Department of Civil and Environmental Engineering, Massachusetts Institute of Technology, Cambridge, MA 02139, USA

^d Department of Mechanical Engineering, Syracuse University, Syracuse, NY 13244, USA

† Electronic supplementary information (ESI) available. See DOI: 10.1039/c6sm01672c

‡ These authors contribute equally to this paper.

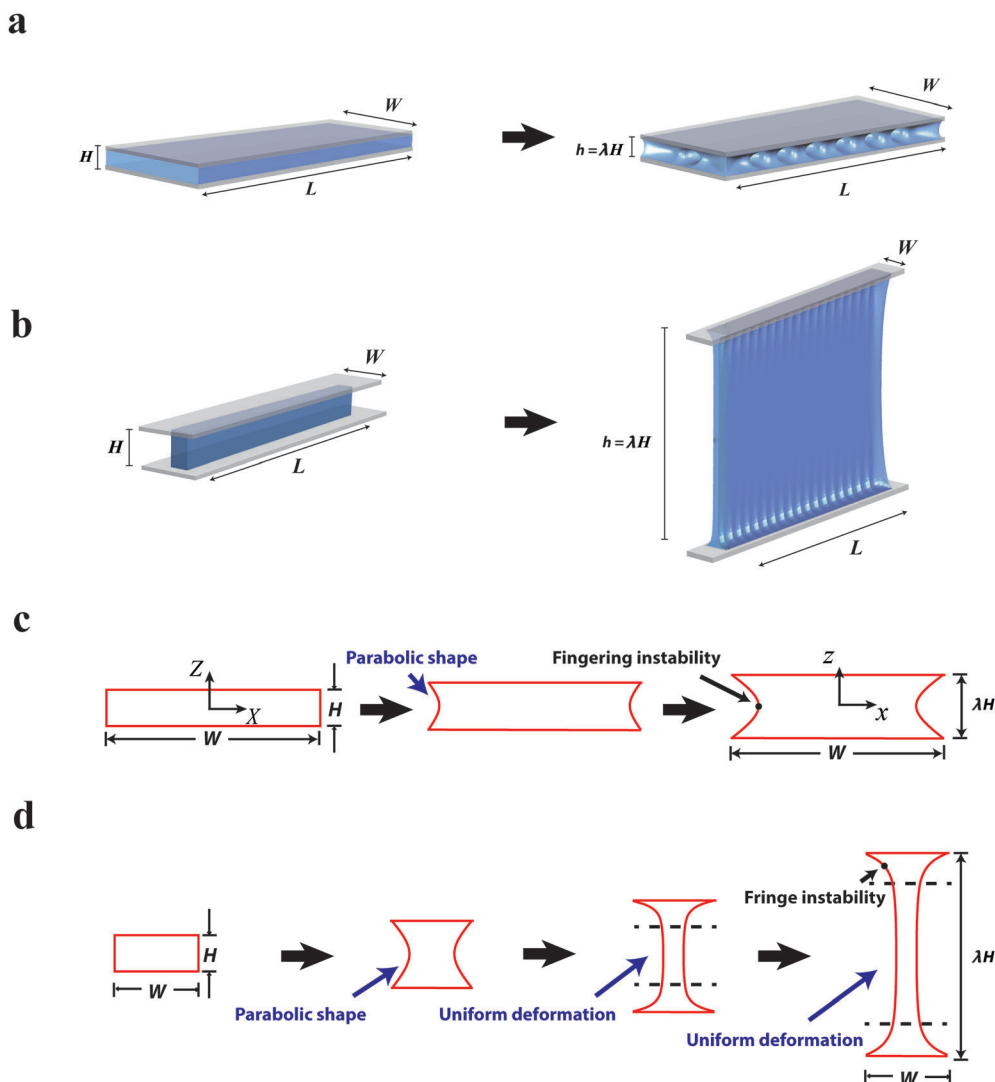


Fig. 1 Schematics of constrained soft elastic layers that undergo the fingering and fringe instabilities. (a) The fingering instability occurs in relatively thin layers (*i.e.*, $W/H > 6$). (b) The fringe instability occurs in relatively thick layers (*i.e.*, $W/H < 3$). (c) Deformation of the exposed meniscus of a relatively thin layer prior to the fingering instability (*i.e.*, $W/H > 6$). (d) Deformation of the exposed meniscus of a relatively thick layer prior to the fringe instability (*i.e.*, $W/H < 3$). Note that the length of the layer is much larger than its thickness in both cases, (*i.e.*, $L/H \gg 1$).

instability, is not parabolic as is the meniscus before fingering instability (Fig. 1c and d). (ii) In load-controlled elongations, the reported fingering instability is associated with a snap-through buckling, which manifests as peaks on the stress-strain curves for relatively thin samples.[§] Such snap-through does not exist in relatively thick specimens, in which the fringe instability dominates. (iii) The critical applied stretch for the onset of fringe instability increases with the decrease of the layer's width–thickness ratio to a finite value of 3.9, which is associated with a constant nominal stress level of 3.8 times of the layer's shear modulus. (iv) The wavelength of the fringe instability scales with the elastic layer's width, but the wavelength of the fingering instability scales with the layer's thickness. The

[§] For brevity, throughout the text we refer to layers of thickness that is much smaller than the in-plane dimensions as 'thin layers', while 'thick layers' are considered to have a thickness of the order of the in-plane dimensions or larger.

discovery of the fringe instability and quantitative comparisons between the fringe and fingering instabilities will advance the current understanding of mechanical instabilities in soft materials and biological adhesives capable of large deformation. Moreover, the fundamental differences in the mechanical response of constrained elastic layers that differ only by their dimensions are expected to be useful in the design and engineering of advanced adhesives and joints,^{6,24} as well as various sealants, insulators and bearings.

2. Experimental details and numerical simulations

Material preparation

To make a soft yet stretchable hydrogel sample, a precursor solution was prepared by mixing 5.5 mL 12 wt% acrylamide

(Sigma, A8887), 4.1 mL 2.5 wt% alginate (Sigma, A2033), 500 μL 0.2 wt% *N,N*-methylenebisacrylamide (Sigma, 146072) as the crosslinker for polyacrylamide and 102 μL 0.2 M ammonium persulphate (Sigma, 248614) as an initiator for polyacrylamide. After degassing the precursor solution in a vacuum chamber, we added 8.2 μL *N,N,N',N'*-tetramethylethylenediamine (Sigma, T7024-50M) as the crosslinking accelerator for acrylamide. The shear modulus of the hydrogel was measured to be 2 kPa, and negligible rate dependence with slight hysteresis was observed in the stress–strain response of the hydrogel under loading–unloading cycles (Fig. S1, ESI[†]).

Experimental setup

The experimental setup used in the current study is illustrated schematically in Fig. 2. A layer of a soft yet stretchable hydrogel was robustly bonded onto two thick and transparent glass substrates.⁶ The width of the hydrogel layer W was varied from 3 mm to 37.8 mm and the thickness H from 1.5 mm to 6 mm, so that the width–thickness ratio of the elastic layer (W/H) was selected in a wide range from 0.5 to 25, in contrast to previous studies focusing on relatively thin sheets (*e.g.*, $W/H \geq 5^{17,18}$). The length of the layer L was fixed to 75 mm, so that $L \gg H$ in all experiments. During a typical test, the bottom glass substrate of the sample was fixed, and the top glass substrate was pulled upward at a speed of 30 mm min^{-1} without causing any lateral displacement, using a universal material test machine (2 kN load cell; Zwick/Roell Z2.5). The applied force was measured by the load cell, and the deformation of the layer's free surfaces was recorded using cameras viewing from two directions (*e.g.*, top view, side view). Owing to the low modulus, high stretchability and negligible defects of the hydrogel^{25–28} and the robust hydrogel–glass interfaces (Fig. S2, ESI[†]),⁶ the cavitation and interfacial instabilities were suppressed in the current experiments. Depending on the width–thickness ratio of the elastic

layer, the exposed free surfaces will deform into different meniscus shapes and then destabilize to exhibit the fingering or fringe undulation patterns (Fig. 1).

Measurement of the meniscus profile

Due to the constrained boundary, the meniscus profile at the visible edge is slightly larger than that in the center part of the sample. To clearly measure the meniscus profile in the center of the sample, we covered the transparent gel with an in-diffusible dye on the lateral free surface of the sample (shown in Fig. S3, ESI[†]). The reason why we chose an in-diffusible dye is to prevent the formation of a fuzzy boundary which may be induced by the diffusible dye.

Numerical simulations

Numerical simulations to capture the deformation and instability of the elastic layer were carried out with the finite element method using ABAQUS/Explicit. Since the effect of water diffusion on the hydrogel is negligible during the time of deformation in the current study,¹⁵ the hydrogel was modeled as a nearly incompressible neo-Hookean material with shear modulus μ and bulk modulus K of 1 kPa and 200 kPa, respectively. This gives an effective Poisson's ratio of 0.497, which is shown to be sufficiently accurate in Fig. S4a (ESI[†]). All numerical models have the same dimensions as the experimental specimens. Symmetric boundary conditions were applied in the mid-plane along the thickness direction and all side surfaces were set to be stress free. A constant velocity along the upward direction was prescribed on the top surface of the elastic layer, and the bottom surface was fixed. A mass scaling technique was used to maintain a quasi-static loading process. The model was discretized with an 8-node linear brick, C3D8R element. The mesh size was taken as small as $\sim 1/10$ of the smallest feature dimension for all samples (*e.g.*, 0.05 mm for $W/H < 2$; 0.1 mm

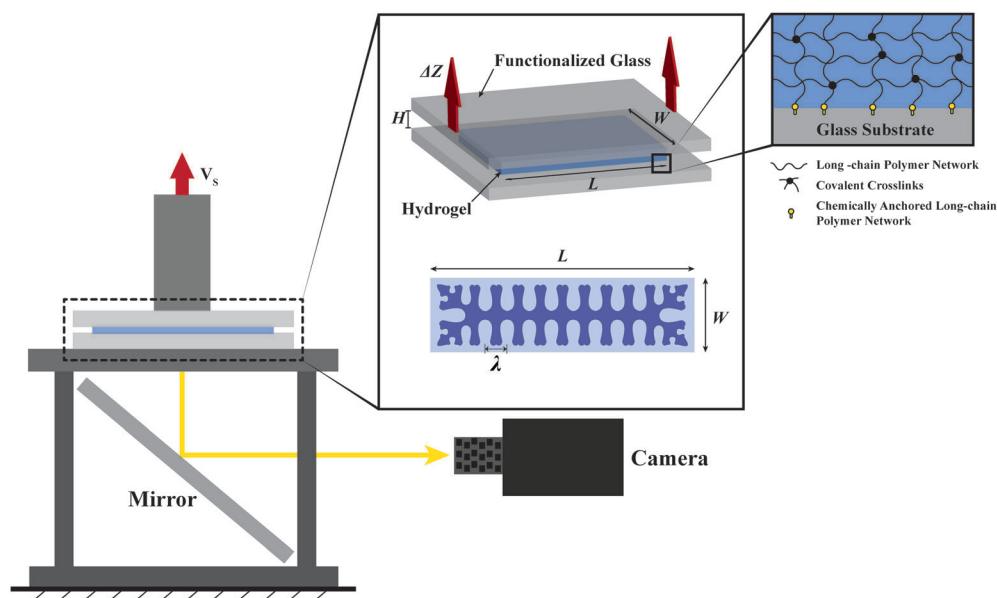


Fig. 2 Schematic illustrations of the experimental setup for the observation of the elastic instabilities in constrained soft elastic layers.

for $2 \leq W/H \leq 4$ and 0.2 mm for $W/H > 4$) to ensure the accuracy of the simulation (Fig. S4b, ESI†).

3. Results and discussion

In both experiments and simulations, the elastic layer with an initial thickness of H is deformed to the current thickness h , and the applied stretch is defined as $\lambda = h/H$. Fig. 1 schematically illustrates the qualitative differences between fingering and fringe instabilities, both of which occur on the exposed meniscus of elastic layers. If the layer is relatively thin or its width–thickness ratio is relatively high (e.g., $W/H > 6$), the deformed meniscus maintains a parabolic shape (Fig. 1c), until a spatially periodic pattern of fingers of air invades the meniscus at a critical

applied stretch λ_c (Fig. 1a).^{17,18} On the other hand, if the layer's width is comparable with or lower than its thickness (e.g., $W/H < 3$), the middle portion of the layer elongates nearly uniformly but the constrained fringe portions deform non-uniformly under relatively high applied stretches (Fig. 1d). As the applied stretch reaches a critical value λ_c , the free surfaces of the fringe portions gradually begin to undulate into a periodic pattern while the middle portion of the layer maintains uniform elongation (Fig. 1b). An exact width–thickness ratio at which the transition between fingering and fringe instabilities occurs cannot be visually detected due to the geometrical similarity in the transition regime ($3 < W/H < 6$). Nevertheless, a clear transition point is observed in the stress–stretch response of the samples as will be explained in light of the experimental, numerical and theoretical results.

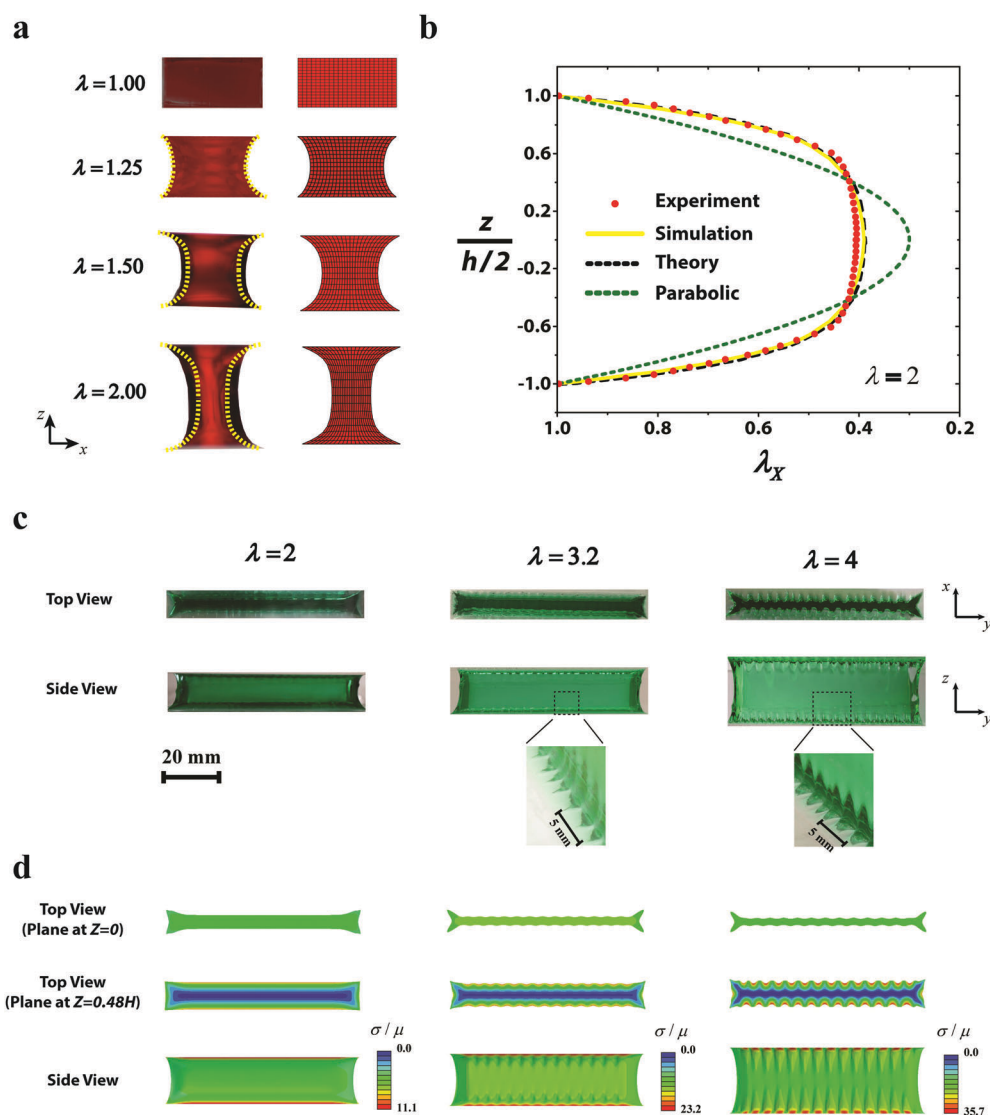


Fig. 3 Experimental, simulation and theoretical results on the deformation and fringe instability in relatively thick layers. (a) Comparison of experimental and simulation results on deformation of a layer with $W/H = 2$ under various applied stretches prior to the fringe instability. (b) Comparison of experimental, simulation and theoretical results on the meniscus shape of a layer with $W/H = 2$ at applied stretch $\lambda = 2$. (c) Experimental observation of the formation of fringe instability for a layer with $W/H = 2$ as the applied stretch increases. (d) Numerical simulation of the formation of fringe instability for a layer with $W/H = 2$ as the applied stretch increases. $\bar{\sigma}$ represents the von Mises stress.

3.1 Meniscus shape prior to instabilities

Fig. 3a and b show both experimental and simulation results for the meniscus shape of an elastic layer with comparable width and thickness (e.g., $W/H = 2$) under various levels of applied stretches, before the onset of any instability. (Due to the effects of front edges in experimental samples, the shape of the experimentally observed meniscus is highlighted by dashed lines. See Fig. S3, ESI† for details on determining the meniscus.) Under relatively low applied stretch (e.g., $\lambda \leq 1.25$), the meniscus of the elastic layer follows the parabolic shape.²⁹ However, as the applied stretch further increases (e.g. to $\lambda = 1.5, 2$), the middle portion of the meniscus elongates uniformly and the constrained fringe portions deform nonuniformly into a V shape (Fig. 3a and b). The shape of the highly-deformed meniscus significantly deviates from the parabolic shape assumed in previous studies on fingering instabilities.^{17,29} From Fig. 3a and b, it can be seen that the numerical model can accurately predict the evolution of the meniscus shape with the increasing stretch (i.e., from parabolic to non-parabolic). In addition, since the middle portion of the layer is uniformly elongated under high applied stretches (e.g., $\lambda = 1.5, 2$), there is no driving force for the formation of fingering instability in the middle portion of the layer in the sample.

Instead, as the soft elastic layer ($W/H = 2$) is stretched to a critical point $\lambda_c \approx 3.2$, the exposed surface of the fringe portions becomes unstable – beginning to undulate periodically while the middle portion of the layer maintains uniform elongation (Fig. 3c and Movies S1, S2, ESI†). If the applied stretch further increases, the undulation in the fringe portions increases in magnitude while maintaining a constant wavelength. The layer maintains adhering on the rigid bodies throughout the process of deformation and fringe instability (Fig. S2, ESI†). Once the applied stretch is relaxed, the elastic layer restores its undeformed state. Evidently, the fringe instability is qualitatively different from the fingering instability that occurs in relatively thin elastic layers (e.g., $W/H = 8$ in Fig. S5 and Movie S3, ESI†). Fig. 3d further shows that the numerical simulation can quantitatively predict the experimental observations of fringe instability. The simulation also confirms that the middle portion of the layer deforms almost uniformly while the fringe portions undergo the instability.

3.2 Theoretical model

Next, we will resort to theory and scaling laws to better understand the experimental and simulation results on the deformation and instabilities in constrained elastic layers with various aspect ratios. While existing studies on fingering instabilities are generally limited to relatively thin layers (e.g., $W/H > 6$) in which the meniscus shape is assumed to be parabolic^{17,30} (Fig. 1c), herein we develop a theory that accounts for the deformation of constrained elastic layers with a wide range of width–thickness ratios and is valid for exceedingly large deformations. Geometrically, the layer in the undeformed state occupies a region $-W/2 < X < W/2$, $-\infty < Y < \infty$ and $-H/2 < Z < H/2$, and a material particle in the layer is labeled by its coordinate (X, Y, Z) in the undeformed state (see Fig. S6, ESI†). In the deformed state, the material particle moves to a place of coordinates (x, y, z) , which

are functions of (X, Y, Z) . We restrict the analysis to plane-strain deformation in the X - Z plane and, without loss of generality, the layer is taken to deform symmetrically with respect to the $Z = 0$ and $X = 0$ planes.

We make a single assumption on the deformation of the layer, that is: any horizontal plane in the layer at the undeformed state remains planar upon deformation³⁰ (see the simulation results in Fig. 3a for validation of the assumption). Based on the above assumption and the incompressibility of the elastic layer, we can express the deformation gradient of the layer as (see detailed derivation in the ESI†)

$$\mathbf{F} = \begin{bmatrix} \lambda_X & 0 & X\lambda_X' \\ 0 & 1 & 0 \\ 0 & 0 & 1/\lambda_X \end{bmatrix} \quad (1)$$

where the in-plane stretch component $\lambda_X = \lambda_Y(Z)$ is independent of the horizontal location, and the superposed prime denotes differentiation along Z . Since the width of the elastic layer at a vertical location Z deforms from W to $\lambda_X W$, we further define λ_X as the meniscus shape function of the elastic layer.

The elastic layer is taken as a neo-Hookean material with strain energy density function $\Psi = \frac{\mu}{2} \text{tr}[(\mathbf{F}\mathbf{F}^T) - 3]$. By minimizing the elastic energy of the layer, the meniscus shape function is found to obey a first-order differential equation

$$\frac{W}{2} \frac{d\lambda_X}{dZ} = \sqrt{3(\lambda_X^2 - \lambda_{X0}^2) + 3(\lambda_X^{-2} - \lambda_{X0}^{-2}) + C(\lambda_X^{-1} - \lambda_{X0}^{-1})} \quad (2)$$

where $\lambda_{X0} = \lambda_X(Z = 0)$ is the meniscus shape function at the vertical mid-point of the layer, and C is a dimensionless integration constant that can be obtained by applying the boundary conditions

$$\lambda_X(Z = \pm H/2) = 1, \quad \lambda = \int_0^{H/2} \frac{2dZ}{\lambda_X H} \quad (3)$$

Solving eqn (2) and (3) yields the meniscus shape function λ_X , deformation gradient \mathbf{F} and elastic energy density Ψ of the layer as a function of the applied stretch λ . The total elastic energy of the layer per unit length in the Y direction, E , can then be calculated by integrating Ψ over the volume of the layer. We further define the averaged nominal stress applied on the layer as the applied force divided by the undeformed horizontal cross-section area, which can be calculated as

$$S = \frac{1}{WH} \frac{dE}{d\lambda} \quad (4)$$

Accordingly we can derive relations between the applied stretch λ , the applied nominal stress S and the meniscus shape λ_X for layers with a wide range of width–thickness ratios. In comparison with both experiments and simulations, it is found that the present analytical solution provides accurate predictions of the meniscus shape even for exceedingly high applied stretches and across the entire regime of specimen dimensions considered in this study. For example we show in Fig. 3b, the meniscus shape of

a layer with $W/H = 2$ at applied stretch of $\lambda = 2$ given by the theory, experiments and numerical simulations. It can be seen that the theory can accurately predict the non-parabolic shape of a relatively thick layer (*i.e.*, $W/H = 2$) under high stretches.

3.3. Transition between fingering and fringe instabilities

Fig. 4 gives the curves of applied nominal stress S vs. applied stretch λ for elastic layers with various width–thickness ratios (*i.e.*, $0.5 \leq W/H \leq 8$); obtained from experiments (Fig. 4a), numerical simulations (Fig. 4b) and eqn (4) of the analytical investigation (Fig. 4c). Depending on the width–thickness ratio of the layer, the S vs. λ curves can be monotonic or non-monotonic. For relatively thin layers (*e.g.*, $W/H = 6$ and 8), where the fingering instability occurs, the S vs. λ curves are not monotonic. The peak values correspond to the critical points S_c and λ_c for the onset of the fingering instability (see Movie S3, ESI†). The non-monotonic S vs. λ relation is consistent with the subcritical nature of the fingering instability.¹⁷ Notably, although the theoretical analysis does not account for the undulated pattern in fingering instability, it can still predict the non-monotonic relations of S vs. λ for relatively thin layers (*i.e.*, $W/H > 5.1$ in Fig. 4c). The area of the middle portion becomes smaller under stretch (Fig. 3a), and the geometrical effect causes the decrease of the nominal stress (Fig. 4c). Analogous to Considère's criterion for necking, the peaks on the theoretical S vs. λ curves (Fig. 3c) indicate a tight upper bound of the critical points for the onset of fingering instability. Since the undulated fingering has lower potential energy than the non-undulated necking predicted by the theory (Fig. S7, ESI†), the fingering instability appears in our experiments and simulations of the samples with relatively thin layers (*i.e.*, $W/H > 5.1$). In addition, the experiments, simulations and theory all show that S_c increases and λ_c decreases with the rise of W/H , which is consistent with previous reports for fingering instability.¹⁷ Notably, the upper-bound critical stretch for the onset of fingering instability obtained from the analytical solution will approach a plateau of 1.4 as the width–thickness ratio increases (Fig. 5c).

On the other hand, for relatively thick layers (*e.g.*, $W/H = 2.5, 2, 1.5, 1$ and 0.5 in Fig. 4), the curves of S vs. λ obtained from experiments, simulations and theory are all monotonic; and the fringe instability is observed in these samples. Strikingly, from both experimental and simulation results, we find that the critical nominal stress for fringe instability in layers with decreasing W/H ratios approaches an approximately constant value of $S_c \approx 3.8\mu$ (Fig. 4b and 5b). Returning to the analytical results in Fig. 4c, and according to the above argument, we may thus obtain an approximate theoretical stability limit by assuming that the fringe instability sets in at the same constant, level of stress from the transition point (where the fingering instability peak vanishes) and to lower width–thickness ratios, as shown by the continuation of the dashed line therein. In addition, different from the subcritical fingering instability,¹⁷ the fringe instability forms gradually with negligible hysteresis on the pattern amplitude vs. applied stretch curves obtained from loading and unloading of the sample (Fig. S9, ESI†).

To identify the critical width–thickness ratio $(W/H)_c$ for the transition between the fingering and the fringe instabilities, we

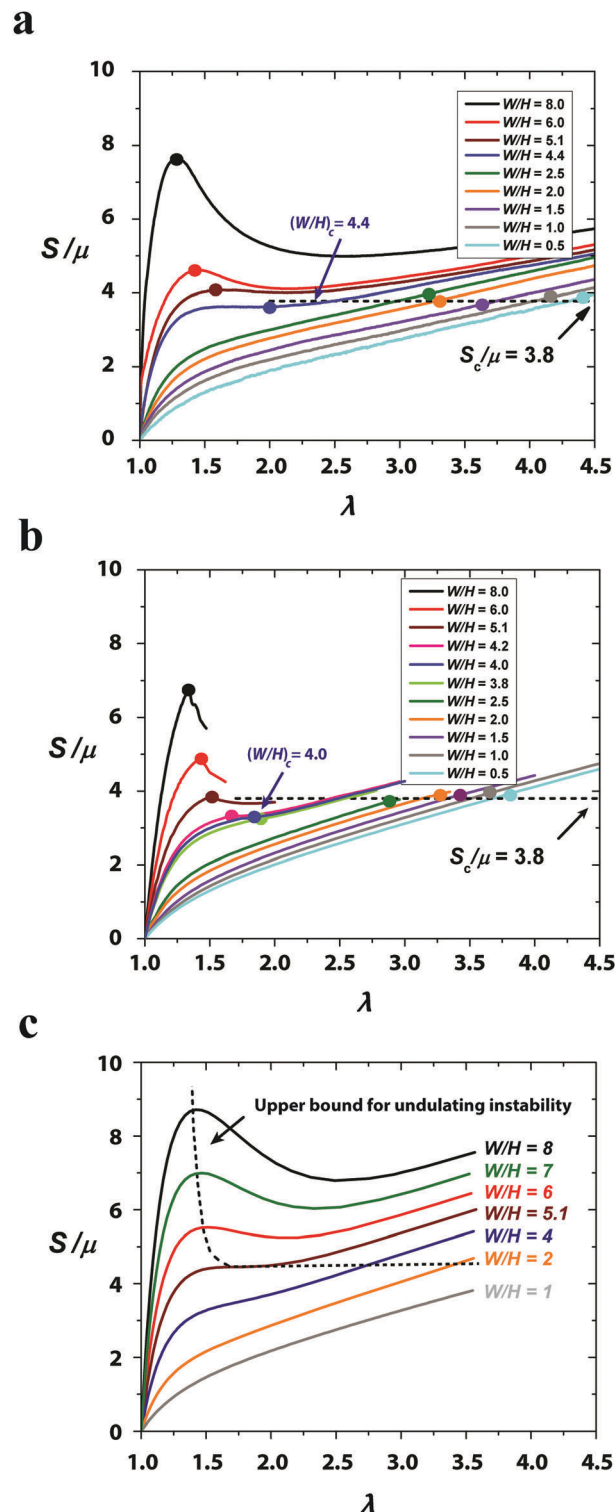


Fig. 4 Experimental, simulation and theoretical results for the applied nominal stress S vs. the applied stretch λ for layers with various width–thickness ratios. (a) Experimentally measured curves of S vs. λ for layers with $W/H = 8, 6, 5.1, 4.4, 2.5, 2, 1.5, 1$ and 0.5 . The critical points for the onset of instabilities are marked on the corresponding curves. (b) Simulation curves of S vs. λ for layers with $W/H = 8, 6, 5.1, 4.2, 4, 3.8, 2.5, 2, 1.5, 1$ and 0.5 . The critical points for the onset of instabilities are marked on the corresponding curves. (c) Theoretical curves of S vs. λ for layers with $W/H = 8, 7, 6, 5.1, 4, 2$ and 1 . The dashed curve represent the stability limit.

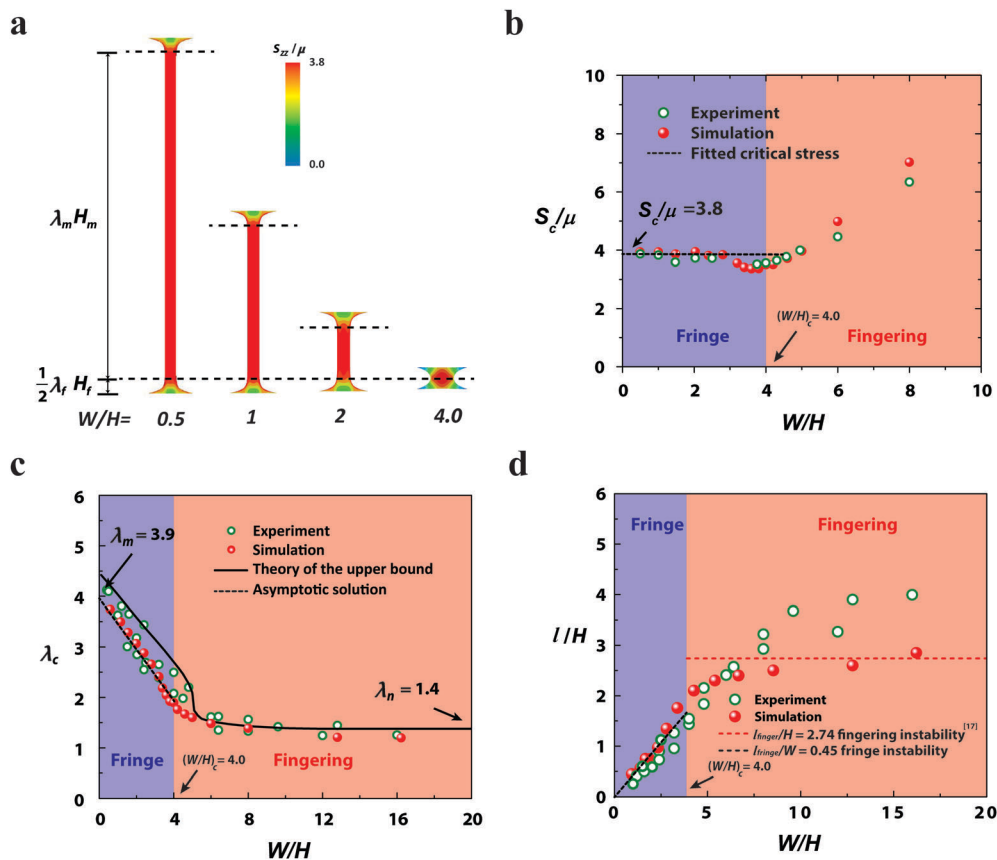


Fig. 5 Experimental, simulation and theoretical results on the characteristics of fingering and fringe instabilities: (a) numerical simulation results on stress contours in layers with $W/H = 0.5, 1, 2$ and 4 right before the fringe instability. The stress represents the normalized nominal stress component along the loading direction S_{zz}/μ . (b) The critical nominal stress for the onset of instabilities in layers with various width–thickness ratios. (c) The critical applied stretch for the onset of instabilities in layers with various width–thickness ratios. (d) The wavelength of instabilities in layers with various width–thickness ratios.

performed a series of experiments and simulations in an intermediate range of width–thickness ratios (e.g., $W/H = 3.8, 4.0, 4.2, 4.3, 4.4, 4.5, 5.1$). As shown in Fig. 4a, the non-monotonic behavior of the nominal stress–stretch curves disappears as W/H decreases to 4.4 in the experiments. In simulations, the critical width–thickness ratio is identified as $(W/H)_c = 4$. This slight difference between the experiment and simulation is possibly due to the deviation of the layer’s mechanical properties from the neo-Hookean model. In this study, we take the simulation result $(W/H)_c = 4$ as the critical width–thickness ratio for the transition between the fingering and fringe instabilities.

3.4 Critical stress, stretch and wavelength for fringe instability

To better understand the characteristics of fringe instability, we plot the nominal stress S_{zz} contours in relatively thick layers (e.g., $W/H = 0.5, 1, 2$ and 4) right before the onset of the fringe instability (Fig. 5a). At this critical point, the middle portion of the specimens is in a state of nearly uniform uniaxial plane-strain tension, which therefore does not cause the fingering instability (Fig. 5a). On the other hand, the fringe portions exhibit a self-similar state of deformation, which is subjected to tensile stress yet constrained by the rigid surfaces. A combination of the tensile stress, mechanical constraint, and material incompressibility

cause the surfaces of fringe portions to undulate, giving the fringe instability.

We denote the thickness of the middle and fringe portions at the undeformed state as H_m and H_f , respectively. Based on the minimum layer thickness for the fringe instability, i.e., $(W/H)_c = 4$, we can further obtain $H_f = W/4$ and $H_m = H - H_f$. At the critical point for fringe instability, the stretch in the fringe portion λ_f is independent of W/H and can be obtained from the simulation results for $W/H = 4$ as $\lambda_f = 1.8$. The critical stretch in the middle portion λ_m is dictated by the nominal stress–stretch relation in plane-strain tension, i.e. $S_c/\mu = \lambda_m - \lambda_m^{-3} = 3.8$, which gives $\lambda_m = 3.9$. Therefore, the asymptotic solution of the critical stretch for the onset of the fringe instability can be expressed as

$$\lambda_c = \frac{\lambda_f H_f + \lambda_m (H - H_f)}{H} \approx 3.9 - 0.52 \frac{W}{H} \quad (5)$$

In Fig. 5c, we summarize the critical stretch levels for both the fringe and fingering instabilities obtained from experiments, simulations and theory. It can be seen that the above linear relation and the simulations can consistently predict the critical stretches for both types of instabilities. The analytical solution further provides a tight upper bound for the critical stretches in the entire range.

While it is known that the wavelength of the fingering instability l_{finger} scales with the elastic layer’s thickness H (Fig. 5d), the

wavelength of the fringe instability l_{fringe} does not follow such scaling since the thickness of the middle portions does not affect the fringe instability wavelength. Instead, the relevant length scale for the fringe instability wavelength is the fringe portion's thickness, which scales with the layer's width. Therefore, the wavelength for fringe instability scales with the elastic layer's width, instead of its thickness. This dependence has been validated by both the experimental and simulation results in Fig. 5d. In addition, by fitting to the experimental and simulation results, we can further obtain the pre-factors for the scales, *i.e.*, $l_{\text{fringe}} \approx 0.45W$.

4. Conclusions

We report a new mode of fringe instability that occurs in a constrained soft elastic layer with one lateral dimension (*e.g.*, width) comparable with or lower than its thickness. Subjected to high stretches, the middle portion of the layer elongates nearly uniformly but the fringe portions deform non-uniformly. At a critical point, the exposed surface of the fringe portions undulates periodically, giving the localized fringe instability. We combine experiments, numerical simulations and theory to quantitatively explain the fringe instability and its differences from the fingering instability, including morphology evolutions, critical stresses and stretches, and wavelengths. We particularly find that the fingering instability represents a global snap-through instability with non-monotonic stress *vs.* stretch relations but the fringe instability is a localized bifurcation mode with monotonic stress *vs.* stretch relations. To our knowledge, the current study represents the first discovery and explanation of the fringe instability in constrained soft elastic layers. On a practical level, our results have implications for the reliability of soft elastic materials bonded on rigid materials; since the occurrence of fringe instability may significantly enhance the stress in the soft elastic materials around the interfaces, likely leading to fracture or debonding of the soft materials. Moreover, understanding the distinct mechanical responses of constrained elastic layers that differ only by their dimensions will help the design and applications of advanced adhesives, joints, sealants, insulators and bearings.

Acknowledgements

This work is supported by ONR (No. N00014-14-1-0528), MIT Institute for Soldier Nanotechnologies and NSF (No. CMMI-1253495). H. Y. acknowledges the financial support from Samsung Scholarship. T. C. acknowledges the support from the MIT-Technion Post-Doctoral Fellowship Program. X. Z. acknowledges the support from NIH (No. UH3TR000505).

References

- 1 K. W. Desmond, N. A. Zaccchia, J. H. Waite and M. T. Valentine, *Soft Matter*, 2015, **11**, 6832–6839.
- 2 N. V. Gohad, N. Aldred, C. M. Hartshorn, Y. J. Lee, M. T. Cicerone, B. Orihuela, A. S. Clare, D. Rittschof and A. S. Mount, *Nat. Commun.*, 2014, **5**, 4414.
- 3 Y. Sun, S. Guo, G. C. Walker, C. J. Kavanagh and G. W. Swain, *Biofouling*, 2004, **20**, 279–289.
- 4 E. Vaccaro and J. H. Waite, *Biomacromolecules*, 2001, **2**, 906–911.
- 5 A. Kinloch, *J. Adhes.*, 1979, **10**, 193–219.
- 6 H. Yuk, T. Zhang, S. Lin, G. A. Parada and X. Zhao, *Nat. Mater.*, 2016, **15**, 190–196.
- 7 C. Creton and M. Ciccotti, *Rep. Prog. Phys.*, 2016, **79**, 046601.
- 8 A. Gent and P. Lindley, *Proc. R. Soc. A*, 1959, **249**, 195–205.
- 9 C. Fond, *J. Polym. Sci., Part B: Polym. Phys.*, 2001, **39**, 2081–2096.
- 10 J. Dollhofer, A. Chiche, V. Muralidharan, C. Creton and C. Hui, *Int. J. Solids Struct.*, 2004, **41**, 6111–6127.
- 11 J. Zhu, T. Li, S. Cai and Z. Suo, *J. Adhes.*, 2011, **87**, 466–481.
- 12 A. Ghatak and M. K. Chaudhury, *Langmuir*, 2003, **19**, 2621–2631.
- 13 J. Chung, K. Kim, M. Chaudhury, J. Sarkar and A. Sharma, *Eur. Phys. J. E: Soft Matter Biol. Phys.*, 2006, **20**, 47–53.
- 14 M. K. Chaudhury, A. Chakrabarti and A. Ghatak, *Eur. Phys. J. E: Soft Matter Biol. Phys.*, 2015, **38**, 1–26.
- 15 A. Chakrabarti and M. K. Chaudhury, *Langmuir*, 2013, **29**, 6926–6935.
- 16 J. Y. Chung and M. K. Chaudhury, *J. Adhes.*, 2005, **81**, 1119–1145.
- 17 J. S. Biggins, B. Saintyves, Z. Wei, E. Bouchaud and L. Mahadevan, *Proc. Natl. Acad. Sci. U. S. A.*, 2013, **110**, 12545–12548.
- 18 K. R. Shull, C. M. Flanigan and A. J. Crosby, *Phys. Rev. Lett.*, 2000, **84**, 3057.
- 19 J. T. Overvelde, D. M. Dykstra, R. de Rooij, J. Weaver and K. Bertoldi, *Phys. Rev. Lett.*, 2016, **117**, 094301.
- 20 P. G. Saffman and G. Taylor, *Proc. R. Soc. A*, 1958, **245**, 312–329.
- 21 G. M. Homsy, *Annu. Rev. Fluid Mech.*, 1987, **19**, 271–311.
- 22 G. H. McKinley and T. Sridhar, *Annu. Rev. Fluid Mech.*, 2002, **34**, 375–415.
- 23 I. Bischofberger, R. Ramachandran and S. R. Nagel, *Nat. Commun.*, 2014, **5**, 5265.
- 24 C. Zhong, T. Gurry, A. A. Cheng, J. Downey, Z. Deng, C. M. Stultz and T. K. Lu, *Nat. Nanotechnol.*, 2014, **9**, 858–866.
- 25 J.-Y. Sun, X. Zhao, W. R. Illeperuma, O. Chaudhuri, K. H. Oh, D. J. Mooney, J. J. Vlassak and Z. Suo, *Nature*, 2012, **489**, 133–136.
- 26 S. Lin, Y. Zhou and X. Zhao, *Extreme Mech. Lett.*, 2014, **1**, 70–75.
- 27 S. Lin, H. Yuk, T. Zhang, G. A. Parada, H. Koo, C. Yu and X. Zhao, *Adv. Mater.*, 2016, **28**, 4497–4505.
- 28 T. Zhang, S. Lin, H. Yuk and X. Zhao, *Extreme Mech. Lett.*, 2015, **4**, 1–8.
- 29 A. Gent and P. Lindley, *Proc. Inst. Mech. Eng.*, 1959, **173**, 111–122.
- 30 W. W. Klingbeil and R. T. Shield, *Z. Angew. Math. Phys.*, 1966, **17**, 281–305.

Supplementary Information

Shaoting Lin^{†1}, *Tal Cohen*^{†2,3}, *Teng Zhang*^{†1,4}, *Hyunwoo Yuk*¹, *Rohan Abeyaratne*¹, *Xuanhe Zhao*^{1,3*}

1. Department of Mechanical Engineering, Massachusetts Institute of Technology, Cambridge, MA 02139;
 2. School of Engineering and Applied Science, Harvard University, Cambridge, MA 02138;
 3. Department of Civil and Environmental Engineering, Massachusetts Institute of Technology, Cambridge, MA 02139; 4. Department of Mechanical Engineering, Syracuse University, Syracuse, NY 13244;
- †. These authors contribute equally to this paper; * To whom correspondence should be addressed.

Email: zhaox@mit.edu

This PDF file includes:

Theoretical model

Supplementary Figures S1 to S9

Captions for Supplementary Videos S1 to S3

Problem setting. Consider a semi-infinite incompressible elastic strip with a rectangular cross-section as illustrated on Fig. S9. A material particle in the layer is labeled by its coordinates (X, Y, Z) in the undeformed state. The undeformed width of the specimen is W and its height H such that the strip occupies the region

$$-W/2 < X < W/2, \quad -\infty < Y < \infty, \quad -H/2 < Z < H/2. \quad (1)$$

The top and bottom surfaces of the strip (at $Z = \pm H/2$) are perfectly adhered to rigid plates while the sides (at $X = \pm W/2$) are traction free. As the rigid plates are drawn away from each other the specimen is stretched to the new deformed thickness h , while the free surfaces retreat to form a meniscus shape to comply with the incompressibility constraint. We denote the spatial coordinate system in the deformed configuration by (x, y, z) and by limiting the analysis to plane-strain deformation patterns we have $y = Y$. Therefore, in the deformed state, the specimen occupies the range

$$-\frac{W}{2}\lambda_X \leq x \leq \frac{W}{2}\lambda_X, \quad -\infty < y < \infty, \quad -h/2 \leq z \leq h/2, \quad (2)$$

where $\lambda_X(Z)$ represents the in-plane stretch of the layer in the X -direction and as such is the normalized meniscus shape which we attempt to find in the present analysis. Here we have anticipated the fact that λ_X is independent of X , a fact that is established below.

Horizontal planes remain planes. The only additional assumption made about the deformation field of the specimen under tensile deformation, is that any horizontal plane in the unloaded state, remains planar and horizontal upon deformation. This assumption was employed in previous studies [1] and, intuitively, is motivated by the fact that both the midplane and the constrained planes necessarily remain planar. Our numerical simulations indicate that this is a good approximation and is not compromised even as the extension progresses and, in fact, the opposite tendency is observed. Note that in compression this assumption holds only in the small strains regime and thus the present study, in pursuit of the large strains response, is limited to tension.

Constitutive response. In the present study we employ the neo-Hookean constitutive model which can be written in terms of the elastic strain energy density per unit volume of undeformed material, in the form

$$\Psi = \frac{\mu}{2} \left(\text{tr}(\mathbf{F}\mathbf{F}^T) - 3 \right), \quad (3)$$

where μ is the shear modulus and \mathbf{F} is the deformation gradient which, for incompressible materials must obey the constraint

$$\det \mathbf{F} = 1. \quad (4)$$

Formulation. Since planes of constant Z are taken to remain planar upon deformation, the vertical coordinate z of any material point depends only on its initial vertical location Z while the in-plane coordinate x may depend on both X and Z . Hence we write the location of a material particle in the deformed configuration in the most general form as

$$x = g(X, Z), \quad y = Y, \quad z = f(Z). \quad (5)$$

Considering perfect adhesion of the specimens to the plates with no rigid motion, we write the boundary conditions

$$f(0) = 0, \quad f(\pm H/2) = \pm h/2, \quad g(0, Z) = 0, \quad g(X, \pm H/2) = X. \quad (6)$$

The deformation gradient \mathbf{F} and the stretch λ_X can now be written in the form

$$\mathbf{F} = \begin{bmatrix} \frac{\partial g}{\partial X} & 0 & \frac{\partial g}{\partial Z} \\ 0 & 1 & 0 \\ 0 & 0 & f' \end{bmatrix}, \quad \lambda_X = \frac{\partial g}{\partial X}, \quad (7)$$

where the prime denotes differentiation with respect to Z . The incompressibility condition in (4) yields the differential equation

$$\frac{\partial g}{\partial X} = \frac{1}{f'} = \lambda_X. \quad (8)$$

Since f is a function of Z alone, it now follows that so is the stretch λ_X . By integrating the above equation and using the boundary condition (6)³ we arrive at the relation

$$g(X, Z) = X\lambda_X. \quad (9)$$

We now insert the relations for g and f in terms of the meniscus shape λ_X back into (7)¹ to write

$$\mathbf{F} = \begin{bmatrix} \lambda_X & 0 & X\lambda'_X \\ 0 & 1 & 0 \\ 0 & 0 & 1/\lambda_X \end{bmatrix}. \quad (10)$$

Hence, for the class of deformations at hand, the problem reduces to finding a single unknown function $\lambda_X(Z)$ with the remaining boundary conditions translated to the form

$$\lambda_X(\pm H/2) = 1, \quad \lambda'_X(0) = 0, \quad \lambda = \int_0^{H/2} \frac{2}{\lambda_X H} dZ, \quad (11)$$

where the second condition is due to symmetry and the specimen stretch is $\lambda = h/H$.

Since the boundary conditions on the traction-free side-surfaces cannot be identically satisfied, we seek a deformation field that minimizes the elastic energy in the system within the class of deformations being considered. The total elastic energy stored in the system is obtained by integrating the energy density (3) over the cross-section of the specimen, which upon inserting the deformation gradient in (10), can be written as

$$E = 2\mu \int_0^{H/2} \int_0^{W/2} (2 - \lambda_X^2 - \lambda_X^{-2} - X^2(\lambda'_X)^2) dX dZ, \quad (12)$$

where we have taken advantage of symmetry. This can be simplified by integration over X :

$$E = \mu W \int_0^{H/2} \left(2 - \lambda_X^2 - \lambda_X^{-2} - \frac{1}{3} \left(\frac{W}{2} \right)^2 (\lambda'_X)^2 \right) dZ - \frac{\mu W C}{6} \left(\int_0^{H/2} \frac{dZ}{\lambda_X} - \frac{h}{2} \right), \quad (13)$$

where the second term incorporates the displacement constraint (11)³ with the Lagrange multiplier C .

To find a function λ_X which minimizes the total energy, we begin by calculating the first variation of the elastic energy E

$$\delta E = 2\mu W \int_0^{H/2} \left(\left(\lambda_X^{-3} + \frac{C}{6} \lambda_X^{-2} - \lambda_X \right) \delta \lambda_X - \frac{1}{3} \left(\frac{W}{2} \right)^2 \lambda'_X \delta \lambda'_X \right) dZ. \quad (14)$$

This can be further simplified via integration by parts to write

$$\delta E = 2\mu W \int_0^{H/2} \left(\lambda_X^{-3} + \frac{C}{6} \lambda_X^{-2} - \lambda_X + \frac{1}{3} \left(\frac{W}{2} \right)^2 \lambda''_X \right) \delta \lambda_X dZ - \frac{2\mu W}{3} \left(\frac{W}{2} \right)^2 \lambda'_X \delta \lambda_X \Big|_0^{H/2}, \quad (15)$$

where, since λ_X is prescribed at $Z = \pm H/2$, we require its variation to vanish there. Moreover the slope λ'_X vanishes at $Z = 0$ according to (11). Therefore the last term in the above relation cancels out and the vanishing of the first variation, $\delta E = 0$, requires

$$\left(\frac{W}{2}\right)^2 \lambda_X'' = 3\lambda_X - \frac{C}{2}\lambda_X^{-2} - 3\lambda_X^{-3}. \quad (16)$$

This can be integrated after replacing $\lambda_X'' = \frac{\partial \lambda_X'}{\partial \lambda_X} \lambda_X'$, to arrive at a separable equation which by integration reads

$$\frac{W}{2} \lambda_X' = (3\lambda_X^2 + C\lambda_X^{-1} + 3\lambda_X^{-2} + D)^{1/2}, \quad (17)$$

where D is an integration constant. Here, in taking the square root, we have chosen the physically relevant branch with positive slope in the midplane. It is instructive to notice from (16) with $\lambda_X = 1$ that the coefficient C is proportional to the curvature of the meniscus shape near the constrained surfaces.

Numerical solution of the above nonlinear differential equation can be obtained by straight forward integration as conducted in the present study via the Runge-Kutta Merson method. To account for all three boundary conditions (11), a shooting method is applied in which the value of C is guessed to iteratively arrive at the required stretch ($\lambda = h/H$). Specifically for the first order equation (17), it is convenient to apply the symmetry boundary condition by defining the in-plane stretch in the midplane by

$$\lambda_X(Z = 0) = \lambda_{X0}, \quad (18)$$

and thus via (11)² it is possible to eliminate D from (17) to write

$$\frac{W}{2} \lambda_X' = (3(\lambda_X^2 - \lambda_{X0}^2) + C(\lambda_X^{-1} - \lambda_{X0}^{-1}) + 3(\lambda_X^{-2} - \lambda_{X0}^{-2}))^{1/2}. \quad (19)$$

A shooting method can then be applied to relate the midplane stretch λ_{X0} to the specimen stretch h/H .

The applied stress. After carrying out the analysis of the previous section, we can insert the deformation field characterized by the single function $\lambda_X(Z)$ back into the energy integral in (12). This allows us to express the stored elastic energy (per unit length) as a function of the specimen's deformed thickness $E = E(h)$. The increment of work (per unit length) invested by the nominal averaged nominal stress S acting on the plates is $WS\delta h$ and this must equal the increment in energy δE :

$$\delta E = WS\delta h, \quad (20)$$

therefore we may write

$$S = \frac{1}{W} \frac{dE}{dh} = \frac{1}{WH} \frac{dE}{d\lambda}, \quad (21)$$

and hence we arrive at the stress-stretch relationship $S = S(\lambda)$.

Figures and Figure Captions

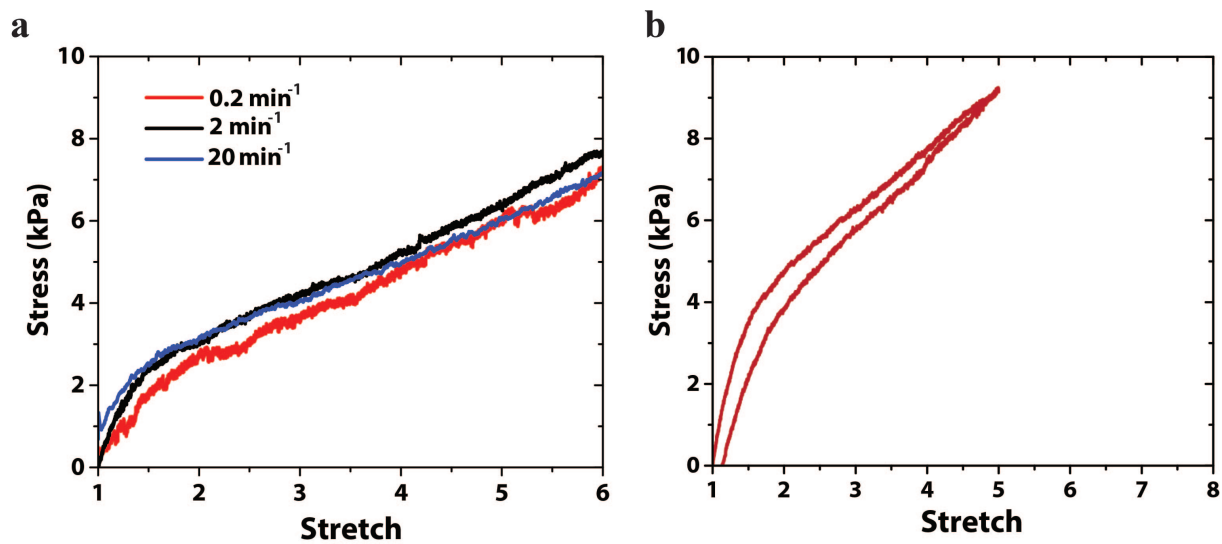


FIG. S1: (a) Monotonic loading at various loading rates; (b) Cyclic loading at the rate of 2 min^{-1} .

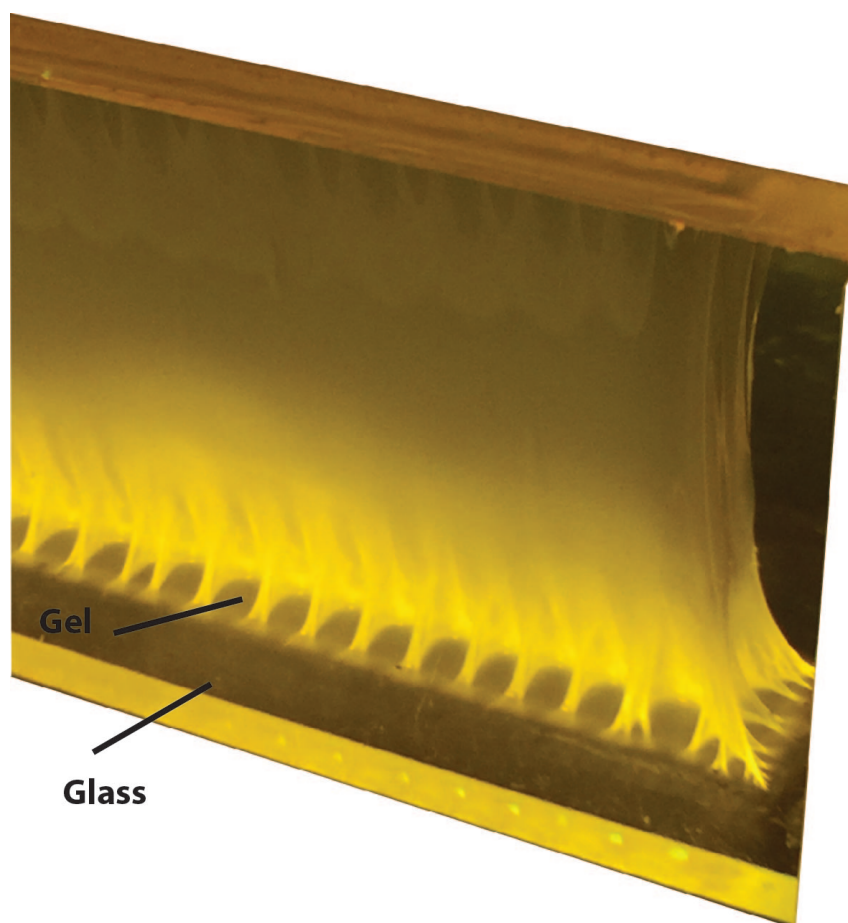


FIG. S2: Fluorescent image of the narrow sample under high deformation with fringe instability forming at the edge. Hydrogel sample with Rhodamine B added is stretched severely. Fringe instability forms at the fixed edge. The fluorescent light in the bounded surface shows the whitish material remaining on the surface, demonstrating perfect interfacial bonding between hydrogel and rigid substrate.

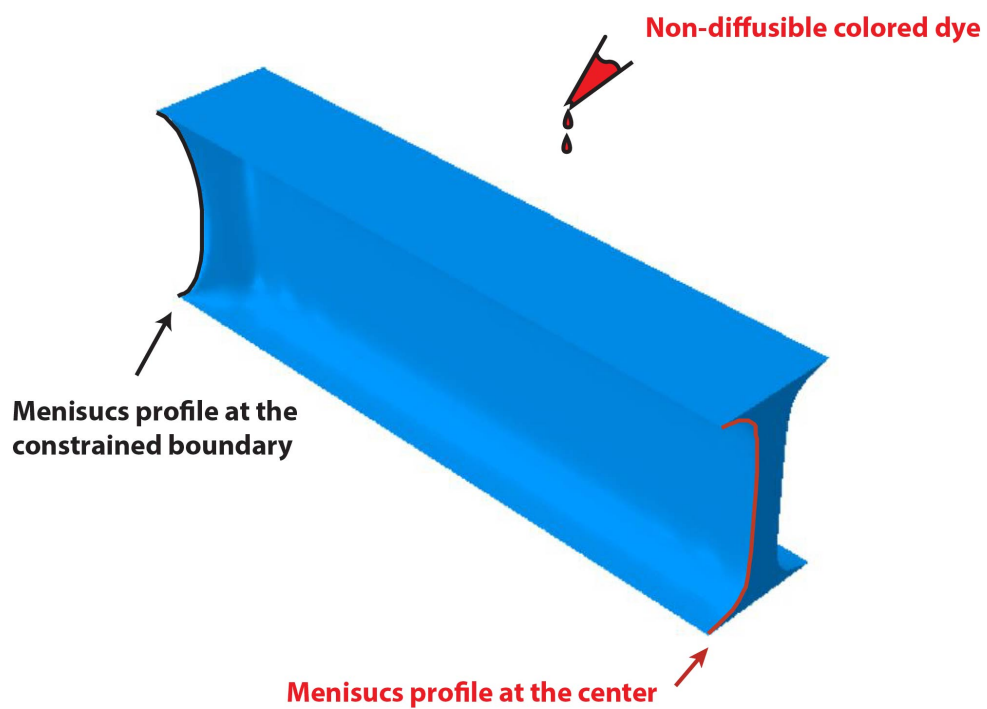


FIG. S3: Non-diffusible colored dye is covered on the surface of transparent hydrogel sample to distinguish with the meniscus profile at the constrained boundary.

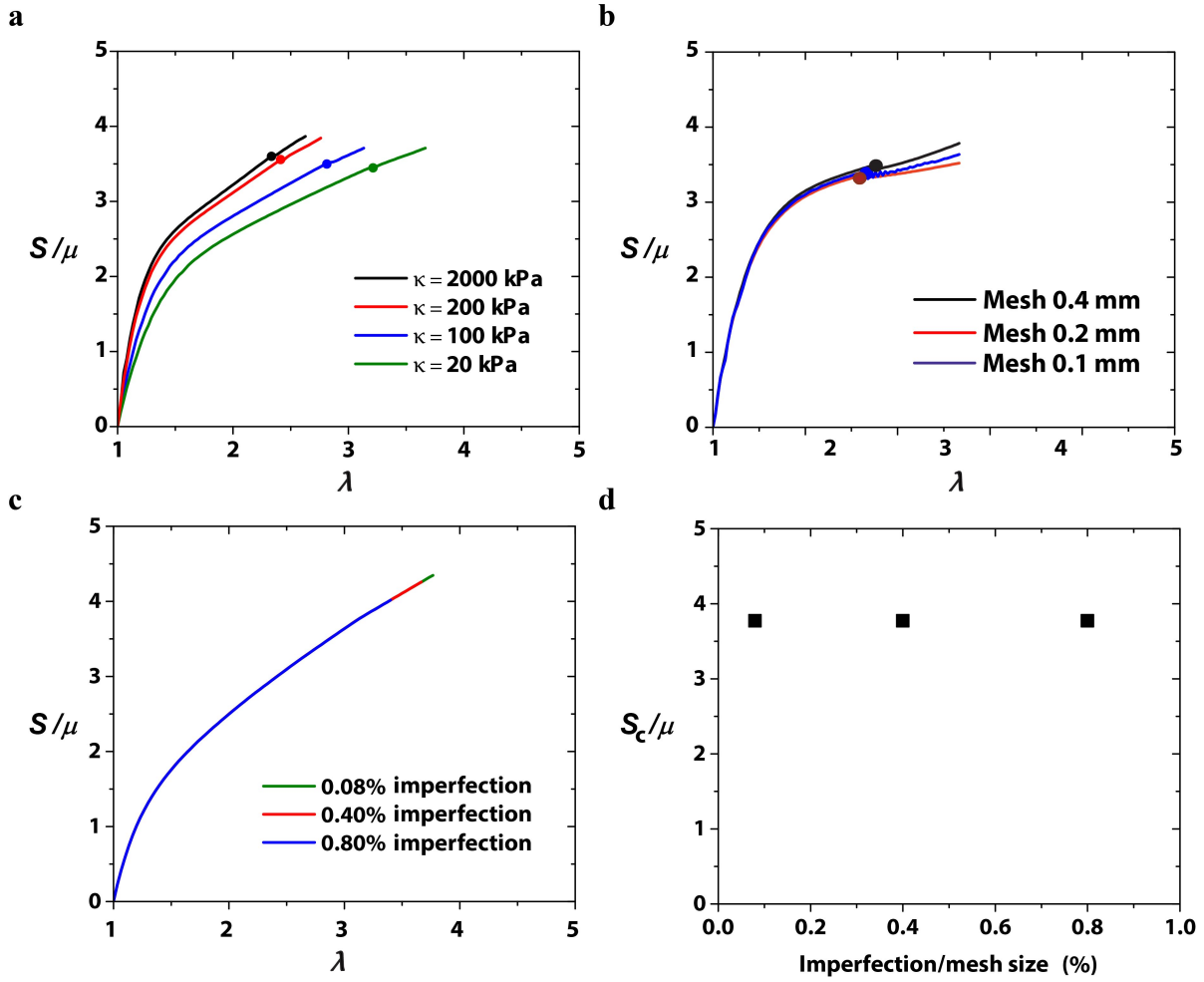


FIG. S4: (a) The nominal stress-stretch curve for the sample with $W/H=3.2$ of various bulk modulus; (b) The nominal stress-stretch curve for the sample with $W/H=4$ of various mesh size; (c) The nominal stress-stretch curve for the sample with $W/H=2$ of various ratios of imperfection to mesh size; (d) The critical stress for the sample with $W/H=2$ of various ratios of imperfection to mesh size.

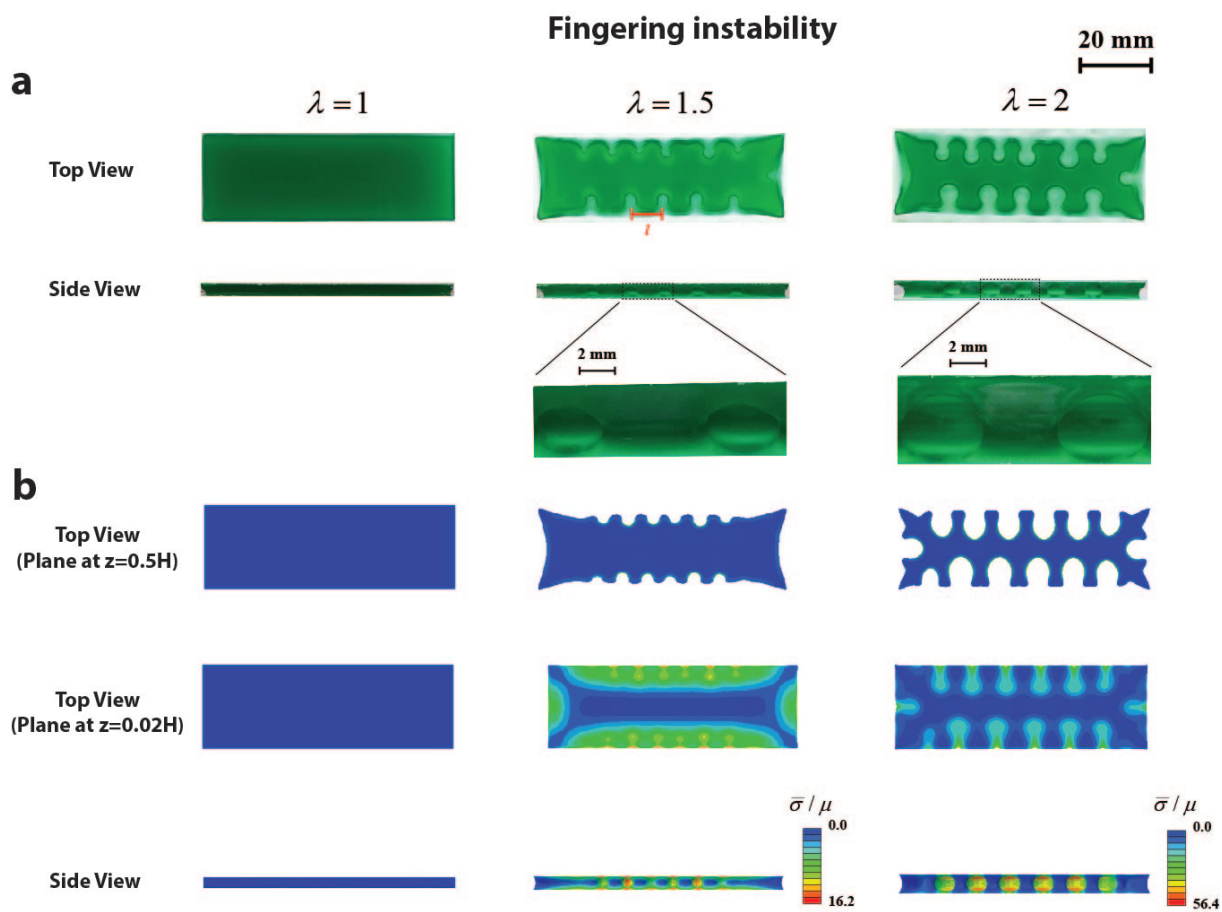


FIG. S5: (a) Experimental observation of the formation of fingering instability for sample with the width-thickness ratio of 2 as strain increases; (b) Numerical simulation of the formation of fingering instability for a sample with identical dimension.

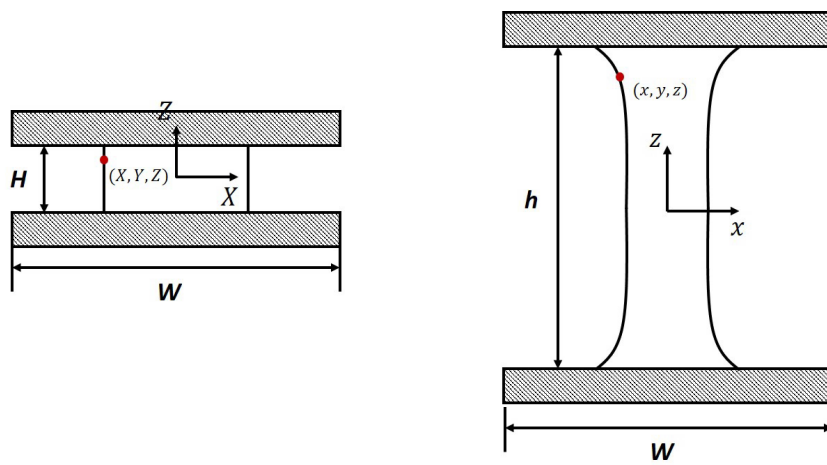


FIG. S6: The cross-section of the specimen in deformed and un-deformed.

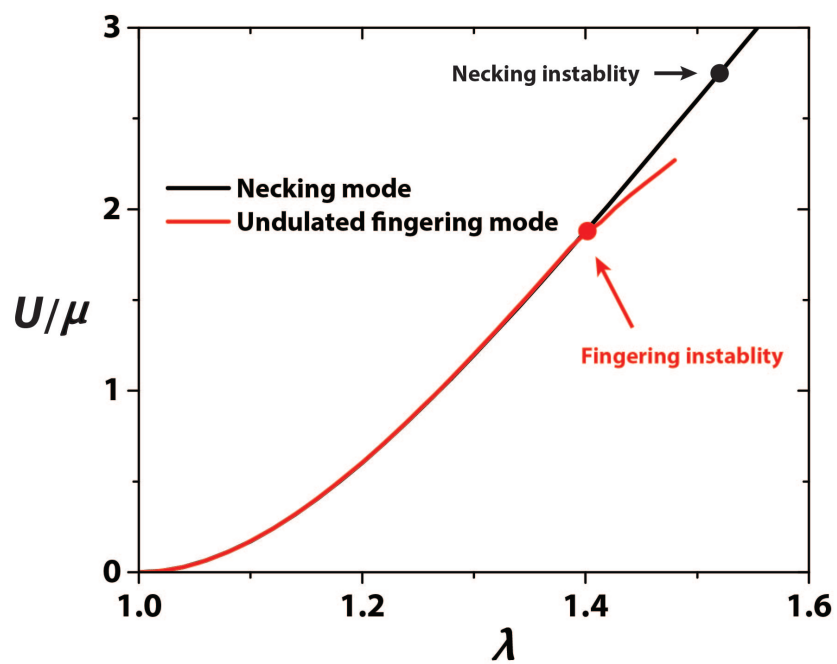


FIG. S7: Comparison of the elastic energy between necking mode and undulated fingering mode for the sample with $W/H = 8$.

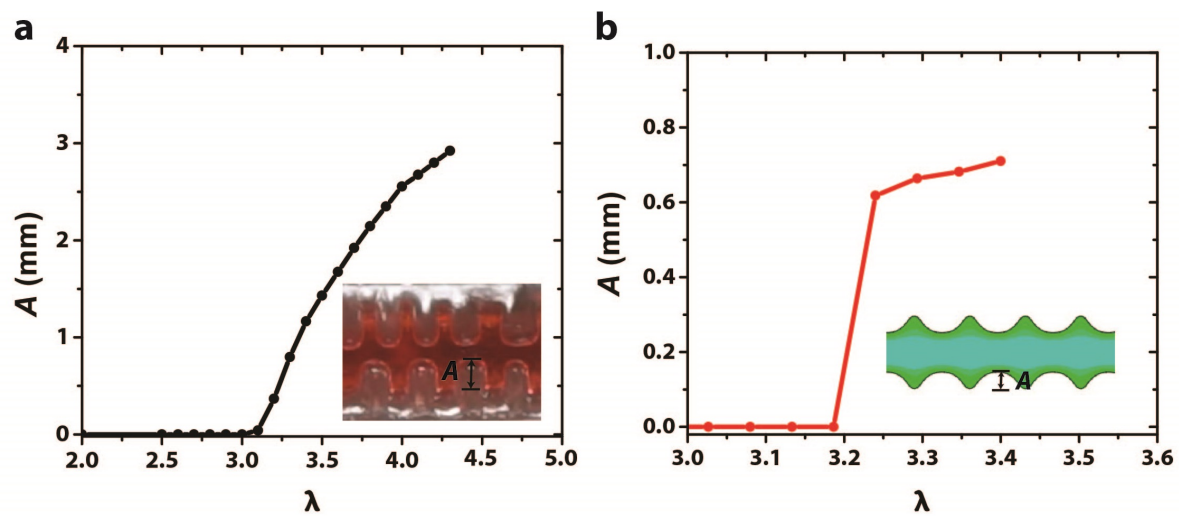


FIG. S8: Amplitude versus imposed stretch for the sample with $W/H = 2$. (a) Measured in experiment; (b) Measured in simulation.

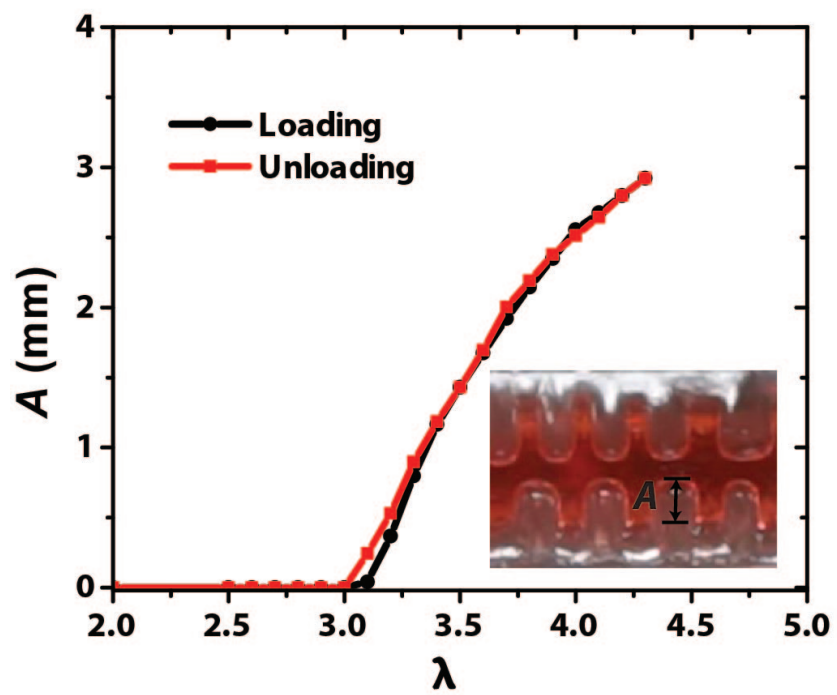


FIG. S9: Loading-unloading curve of amplitude versus imposed stretch for the sample with $W/H = 2$.

Captions for Supplementary Videos

Supplementary Videos S1

Top view and side view of the formation of the fringe instability for the sample with $W/H = 2$.

Supplementary Videos S2

Simulation of the formation of the fringe instability for the sample with $W/H = 2$.

Supplementary Videos S3

Top view and side view of the formation of the fingering instability for the sample with $W/H = 8$.

[1] Werner W Klingbeil and Richard T Shield. Large-deformation analyses of bonded elastic mounts. *Zeitschrift für angewandte Mathematik und Physik ZAMP*, 17(2):281–305, 1966.